

Spectroscopy of molecular hydrogen in outflows from young stars^{*}

J. Eislöffel¹, M.D. Smith², and C.J. Davis^{3,4}

¹ Thüringer Landessternwarte Tautenburg, Sternwarte 5, 07778 Tautenburg, Germany

² Armagh Observatory, College Hill, Armagh BT61 9DG, Ireland

³ School of Cosmic Physics, Dublin Institute of Advanced Studies, 5 Merrion Square, Dublin 2, Ireland

⁴ Joint Astronomy Centre, 660 N. A'ohoku Place, University Park, Hilo, HI 96720, USA

Received 20 March 2000 / Accepted 23 May 2000

Abstract. We present new medium-resolution longslit spectra in the near-infrared and examine the excitation of molecular hydrogen across several outflows from young stars. In contrast to previous studies, in which the brightest patches in the flows were selected, we find evidence for variations in excitation with position within several sources.

We present and comment on a number of H₂ excitation mechanisms of outflows from the literature, and compare them with our observations. H₂ position-velocity diagrams and line ratios support a picture in which the excitation variations are caused by the large-scale shock geometry. The variations are best interpreted by magnetohydrodynamic C-shocks, although some locations which demonstrate hydrodynamic J-type excitation are found. In particular, VLA 1623 is accurately modelled by a C-type bow, whereas a planar J-type model is favoured for HH 57. HH 1/2 consists of a collection of molecular bow and planar shocks. The H₂ emission from the leading edge of the HH 1 bow structure is actually from a low-excitation oblique wing from one of many mini bow shocks rather than from fluorescence or a magnetic precursor.

In two of our objects, the jets themselves are also traced in molecular hydrogen emission. Radial velocities in the infrared jet in HH 47C demonstrate acceleration consistent with the proper motions, and hint at ballistic motions originating in an eruptive event about 280 years ago. In this jet, as well as in the HH 1 infrared jet, we find the excitation to decline with distance from the source.

Key words: shock waves – molecular processes – stars: mass-loss – ISM: jets and outflows – ISM: kinematics and dynamics – ISM: molecules

1. Introduction

Protostellar outflows are collimated supersonic flows of gas which accompany the birth of stars. They can be studied by analysing the radiative shock waves generated within their driv-

ing jets or at their zones of impact with their environments. The shocks produce prominent signatures at infrared wavelengths. In particular, strong line emission is produced from the hydrogen molecule through vibrational and rotational transitions. Here, we employ these transitions to determine the excitation state of the gas in several outflows emanating from various young stars.

Our objectives are as follows. First, the outflows are laboratories for exploring supersonic molecular dynamics and molecular shock physics. Our results will help us understand the dynamics of molecular clouds and the dissipation of supersonic turbulence in star forming regions. Second, we can directly explore the physical conditions within outflows, their means of propagation and the means of momentum transfer into the ambient medium. We may eventually employ the shock emission as a measure of the recent energy output of an outflow and thus have a new parameter to track protostellar evolution.

This study is intended to extend upon previous low spatial resolution studies of large outflow regions, as well as a few high resolution studies of individual bow shocks. Our intent was to observe several K-band lines of H₂ at several positions within each outflow, which then places constraints on the underlying shock physics and outflow dynamics. Low resolution studies have revealed a surprisingly narrow range of excitations (Burton et al. 1989, Gredel 1994). High resolution studies of bright H₂ outflows have also uncovered quite uniform excitation (Davis & Smith 1995, Eislöffel et al. 1996). Is there some self-regulating excitation mechanism, or were the results subject to selection criteria? With these deeper spectra in which faint and bright emission features are examined, we can answer this question. Hence, we have chosen regions within which we can detect fragments of bow shocks plus shells and outflows of considerably different protostellar and dynamical ages.

2. Observations and data reduction

We have taken medium-resolution ($\lambda/\Delta\lambda = 2000$) longslit spectra in HH 1/2, HH 46/47, HH 57, VLA 1623, and NGC 6334I with IRSPEC at the ESO/NTT on La Silla (Chile) in December 1994 and in May 1995. A summary of all our spectroscopic observations is given in Table 1. The instrument uses a SBRC InSb array of 58×62 pixels, with a pixel scale of 2''/2 per pixel. In December 1994 we used a slit width of 5''/5,

Send offprint requests to: J. Eislöffel

^{*} Based on observations collected at the European Southern Observatory, La Silla, Chile.

Table 1. Observing log

Object + Slit	Date	P.A.	Note
HH 1/2 I	20.12.1994	-41°3	
HH 1/2 II	18.12.1994	-33°8	
HH 1/2 III	19.12.1994	-53°3	
HH 1/2 IV	19.12.1994	+128°1	
HH 46/47 I	19.12.1994	+46°2	
HH 46/47 II	20.12.1994	+69°1	*
	10.05.1995	+69°1	
HH 46/47 III	20.12.1994	-126°5	*
	9.05.1995	-126°5	
HH 57	10.05.1995	+18°7	
NGC 6334I	10.05.1995	+50°2	
VLA 1623	10.05.1995	-97°8	

* These slit positions were observed under less favourable weather conditions and are not shown here.

while a slit width of 4''4 (2 pixels) was employed in May 1995. The array covers a wavelength range of about 0.026 μm in the K-band, varying with wavelength. Therefore, spectra in several grating positions had to be taken to cover the observed lines. They were taken with an interleaving strategy in order to allow for checking the stability of the line ratio measurements. Several object-sky-sky-object groups with 60 sec integration time per position were observed, for a typical total integration time of 10 min per slit position.

The spectral images were sky-subtracted, flatfielded, straightened, wavelength- and flux-calibrated using the IRSPEC context in MIDAS. In December 1994 β Ori, γ Ori, and β Car were used as flux-calibrators, while β Car and η Oph were used in May 1995. Velocities of the H_2 gas were measured relative to the OH (9,7) $\text{R}_1(1)$ line at 2.12440 μm (Oliva & Origlia 1992) and converted to systemic velocities.

3. Diagnostic background

3.1. Excitation of H_2 and the Column Density Ratios (CDR)

The information available from our observations are: (1) several H_2 emission line fluxes F_j , (2) the radial velocity V_r of the 1-0 S(1) line and (3) the spatial structure of the 1-0 S(1) emission. The excitation test discussed here uses just the fluxes. To extract the H_2 excitation properties, we convert the fluxes into Column Density Ratios (CDRs) (Brand et al. 1988). A CDR diagram is then a convenient and accurate means of displaying a wide range of excitations. It is derived as follows.

For the analysis, we require several well-known constants: the transition wavelengths λ_j , the temperatures of the upper level of the transitions T_j , the rotational statistical weights of the upper levels $2J_j+1$, and the radiation coefficients E_j . We also require the average extinction at each location and line wavelength, A_j and the H_2 ortho:para ratio ϕ . Then we can

derive the intrinsic (beam-average) column of gas in the upper level of the transition N_j :

$$N_j = 10^{0.4A_j} \frac{4\pi\lambda_j F_j}{hcE_j\theta^2} \quad (1)$$

where θ^2 is the aperture or beam size in radians. We denote the relative column as

$$C_j = N_j/N_{1,3} \quad (2)$$

where $j = (1,3)$ is the upper level of the 1-0 S(1) transition which produces the strong K-band line.

The CDR method compares the relative columns with those produced from a gas in local thermodynamic equilibrium (LTE) at $T_o = 2000$ K with $\phi_o = 3$, i.e. with the normalised columns $C_j^o = N_j^o/N_{1,3}^o$ where

$$N_j^o = \psi_o N(\text{H}_2) \frac{(2J_j + 1) \exp(-T_j/T_o)}{Z(T_o)} \quad (3)$$

with the partition function (Smith et al. 1997a)

$$Z(T) = 6.13510^{-3} T [1 - \exp(-5850/T)]^{-1} \quad (4)$$

and $\psi = \phi/(1 + \phi)$ for an ortho transition and $\psi = 1/(1 + \phi)$ for a para transition.

The quantity we will actually plot against T_j is defined as

$$\log(CDR_j) = \log(C_j/C_j^o). \quad (5)$$

The advantages of this method are (1) $\log CDR_j$ would be zero (i.e. $C_j/C_j^o = 1$) if we were observing a slab of temperature T_o , so the diagrams display sensitively the variations from this temperature and (2) $\log(CDR_j)$ is a linear function of T_j for any constant temperature gas (the slope of the line being dependent on the temperature).

An excitation temperature can be defined between any two transitions given their columns and the ortho-para ratio:

$$T_{jk} = (T_k - T_j) \ln \left[\frac{\psi_j(2J_j + 1)N_k}{\psi_k(2J_k + 1)N_j} \right]. \quad (6)$$

Extinction is estimated here from the 1-0 Q(3)/1-0 S(1) ratio. Since these two transitions share the same upper energy level, their intrinsic ratio is a physical constant. Hence only extinction and observational uncertainties (telluric absorption, instrument sensitivity, line blending) can influence this ratio. It should be noted that in no position do we find an extinction which alters the CDRs sufficiently to influence derived excitation temperatures more than $\sim 10\%$. Although in many positions the extinction cannot be accurately measured, we still assume the extinction given by the quoted mean fluxes (provided it is positive).

Two remarks should be made here. First, the comparison to a gas in LTE provides information on the density and temperature. LTE is expected at very high densities, the critical value depending on the ro-vibrational state being considered and the fraction of atomic hydrogen available (which, according to calculated collision rates, can dominate the H_2 excitation). Secondly, the ortho:para ratio can usually be taken as 3 within Herbig-Haro objects (Smith et al. 1997a). Deviations would be recognisable in terms of distinct CDR- T_j curves for each vibrational level and H_2 modification.

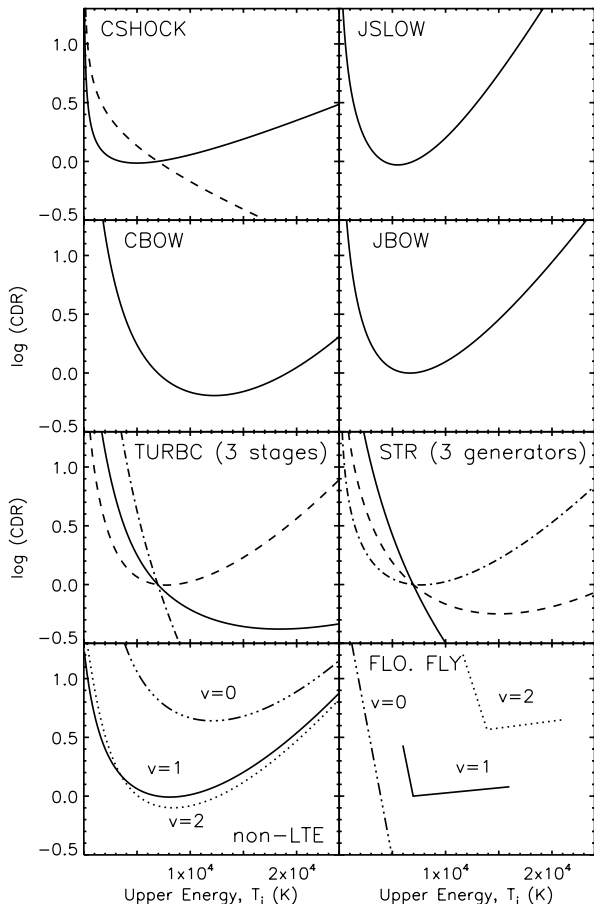


Fig. 1. Schematic CDR diagrams to illustrate many of the possible excitation properties of molecular hydrogen from established and new models.

3.2. Excitation models for the H_2 gas

A multitude of excitation mechanisms have been proposed for H_2 in outflows and Photodissociation Regions by many authors. Simulated CDR diagrams have been calculated for many of these excitation models. The properties of these models are discussed here and summarised in Fig. 1.

Model ITEMP. A reservoir of constant temperature gas. Assuming LTE, this produces a single straight line on the CDR diagram, the gradient yielding the excitation temperature. We use this method when we have detected only a few 1-0 and 2-1 lines, which do not warrant detailed modelling (see also Garnavich et al. 1997). The model is physically implausible since no scenario has been assembled in which molecular gas can be held at a fixed temperature within the relevant range of 1000–4000 K (a planar C-shock gets the closest). It is, however, suitable as a diagnostic when insufficient data is available for detailed comparison with dynamical models and can thus provide a constraint when compared to molecular hydrogen excitation tables (e.g., Smith 1995).

Model NTEMP. Several constant temperature components co-existing. By fitting N straight lines to N temperature ranges of a CDR plot, one obtains diagnostics for dynamical models,

as well as identifying non-thermal physics (ortho-para variations, fluorescence, reformation). The plausibility of this model is low since there are no equilibrium temperatures or multi-phase media expected in the temperature range in which H_2 is detected. Apparently successful two-temperature fits to the H_2 peak in Orion (Everett et al. 1995, not using the CDR method), are not viable on sensitive CDR plots (Burton & Haas 1997). This will undoubtedly also apply to the two-temperature fits made by Ayala et al. (1998) to their recent observations of the IRAS 20126+4104 outflow.

Model CSHOCK. A planar C-type shock, in which ion-neutral friction heats the gas in a thick shock layer (Draine, Roberge & Dalgarno 1983). The CDR has only slight curvature. Note that the apparently good CSHOCK models, which interpret limited OMC-1 data (Draine & Roberge 1982), have been discounted by more extended data sets (Smith & Brand 1990a). The excitation temperature of a C-shock is sensitive to the density, ion fraction, magnetic field strength, magnetic field direction, shock speed and oxygen chemistry (Smith & Brand 1990b). These parameters cannot be uniquely extracted through modelling. Plausibility: high only if all the above parameters remain uniform over the observed region.

Models CT. Time-dependent C-shocks. Planar C-shocks with moderate to high Alfvén numbers (> 5 for a transverse field) are unstable (Model CTU) (Wardle 1990). Instability alters the resulting CDR behaviour by increasing the quantities of hot and cold gas, steadily increasing the CDR curvature (Fig. 16 of Mac Low & Smith 1997). The time scale is about one third of the flow time scale ($\sim 20/(n_i/1 \text{ cm}^{-3})$, where n_i is the ion density). Curvature is a common feature on CDR diagrams, but no time sequences are as yet available. Furthermore, variations may be washed out since these are uncorrelated variations over the shock surface on the scale of the shock width.

Model PREC. Magnetic precursor to fast or slow planar J-type shock. C-shocks require considerable times to form. The time to reach the steady state CDR (Fig. 12 of Smith & Mac Low 1997) beginning from a jump shock structure is about one flow time. During this time, a precursor develops, producing quasi-linear CDRs (Smith & Mac Low 1997). An equivalent bow precursor could thus produce curved CDR. Parameters which yield a steady-state precursor remain to be found and may not be significant. In fast shocks it is clear that pre-shock ionisation kills the magnetic precursor. Precursors may, however, be prevalent as shocks are continually evolving.

Model CBOW. A curved C-type shock. Convex CDR curves are produced. The CDR curve is independent of the bow speed provided the speed exceeds the molecular breakdown speed (i.e. the bow apex corresponds to a hot dissociated cap and the H_2 emission is distributed in fixed warm, cool and cold components in the wings). Then, CDR curves depend only on the bow geometry, departure from LTE, and the oxygen abundance (Smith et al. 1991a, 1991b). Low excitation temperatures are predicted for the rotational excitation (~ 300 – 1000 K, low 0-0 ratios) and for 1-0 ratios (~ 1000 K), while moderate excitation from 2-1/1-0 ratios (1500–2500 K) are generally predicted for paraboloidal

bows. More aerodynamic bows have been suggested by the overall lower excitation in Cepheus E (Eislöffel et al. 1996).

Model TURB. Supersonic turbulence is generated by a jet or wind in some initial impulse. The turbulence is then left to form shocks which then dissipate, interact and disperse (see e.g. DR 21 for an observed example; Davis & Smith 1996). The shock spectrum is an exponential function of velocity and time which suggests that weak shocks dominate the molecular excitation properties. Both J-type, TURBJ, and C-type, TURBC, versions would thus predict low excitation (Smith et al. 2000a).

Model STR. A presumed quasi-steady velocity cascade, termed a ‘Supersonic Turbulent Reactor’ results when uniformly driven turbulence (Smith et al. 2000b) dissipates energy in the resulting spectrum of shocks (Smith et al. 2000c). At work in the shear layers in radiative bow shocks and in their wakes. Curved CDRs are generated, similar to Model TURB, depending on the driving energy. Full details are in preparation (Smith et al. 2000c).

Model JSLOW. Non-dissociative planar radiative shocks. High excitation CDR curves (3000–3600 K) are predicted under the most probable conditions. Lower excitations are only possible with a high magnetic field or a carefully chosen shock velocity (Smith 1994). Plausibility: requires reasonably high ion/neutral fraction ($\chi > 10^{-5}$).

Model JFAST. A dissociative front is followed by cooling and molecule reformation at $T \sim 500$ K. No detailed CDRs are available. However, this model is characterised by high 2-1 S(1)/1-0 S(1) ratio, low intensities and cascade signatures (i.e. strong fluorescence lines, Hollenbach & McKee 1989). Also immediately distinguished by the strong atomic hydrogen emission (including the infrared lines Br γ , P β etc.).

Model JBOW. A curved J-type shock in which molecular emission is dominated by extended wings of Model JSLOW type (Smith 1994). Plausibility: to reduce the excitation to levels often observed requires extremely long weak shock sections.

Model FLO. X-ray and UV radiation heats and excites the molecules by UV pumping, via electron collisions and by direct dissociation and consequent reformation. A fluorescent spectrum is produced. Each vibrational level produces a distinct CDR curve, with higher levels generating larger columns (e.g., McCartney et al. 1999). This contrasts with shocks from within low density gas (i.e. non-LTE) in which the CDRs for higher vibrational levels are depressed (see Fig. 1). Further variation is caused by a non-thermal ortho-para ratio. The result is a possible low temperature CDR component in the low vibration levels plus numerous strong transitions stemming from high vibrational levels. The predicted spectrum (Black & van Dishoeck 1987) has been confirmed in various Photon Dominated Regions (e.g. Ramsay et al. 1993).

Model FLY. UV radiation from nearby shocks excites the molecules by Lyman resonance excitations (possibly in addition to Model FLO; Black & van Dishoeck 1987). Description: besides the Model FLO CDRs, the 2-1 S(3) and S(4) levels could be selectively depopulated (Neufeld & McKee 1988). This effect, however, has not as yet been observed. Model FLY may also occur in conjunction with bow shock models, with the

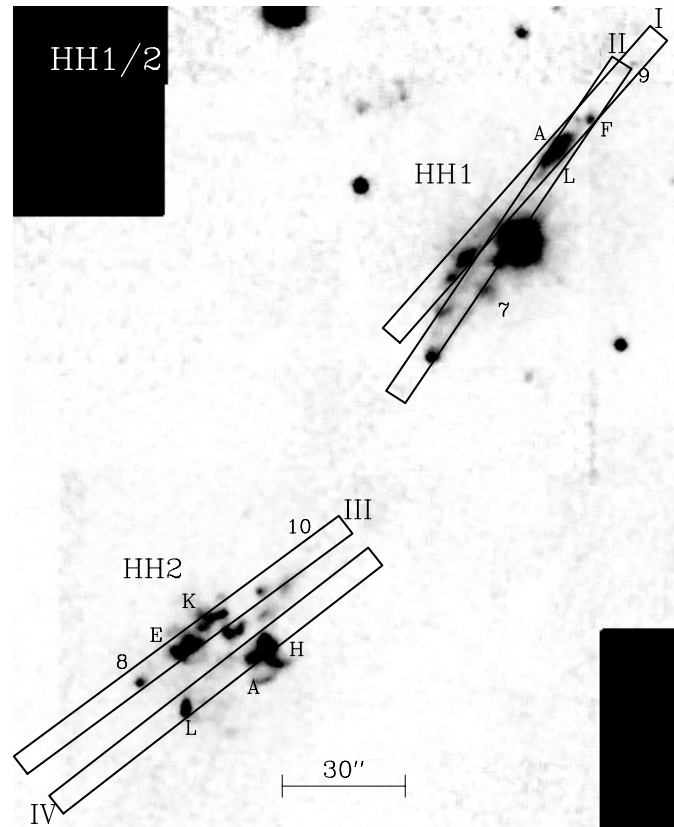


Fig. 2. Observed slit positions in HH 1/2 on an image in the 1-0 S(1) line of H₂ at 2.12 μ m. Roman numerals indicate the orientation of the slits (this end appears at the top in Fig. 3.)

Ly α emission arising from the strong shocks across the bow cap (Fernandes & Brand 1995).

To distinguish between some of these models requires H₂ fluxes with high signal-to-noise from transitions that span a wide range of upper level temperatures. Although currently such data is not always available, we find below that when the data are of sufficient quality many of these models can be excluded in specific knots.

4. Results

4.1. HH 1/2

The morphology of HH 1/2 in the 1-0 S(1) line of molecular hydrogen has been studied by Davis et al. (1994) and by Noriega-Crespo & Garnavich (1994). Noriega-Crespo et al. (1997) have also measured proper motions for three H₂ knots in HH 1, and found motions comparable to those seen in the optical HH emission knots. Spectroscopy in the K-band, and a study of the excitation of the H₂ gas in HH 1 has been presented by Gredel (1996), and in HH 2 by Schwartz et al. (1995).

The image presented in Fig. 2 gives an overview over the HH 1/2 region in the 1-0 S(1) line of H₂ at 2.12 μ m. The positions of our four IRSPEC longslits are indicated and numbered. Continuing the numbering scheme of Davis et al. (1994), we name two fainter knots 9 and 10, which can be clearly identified

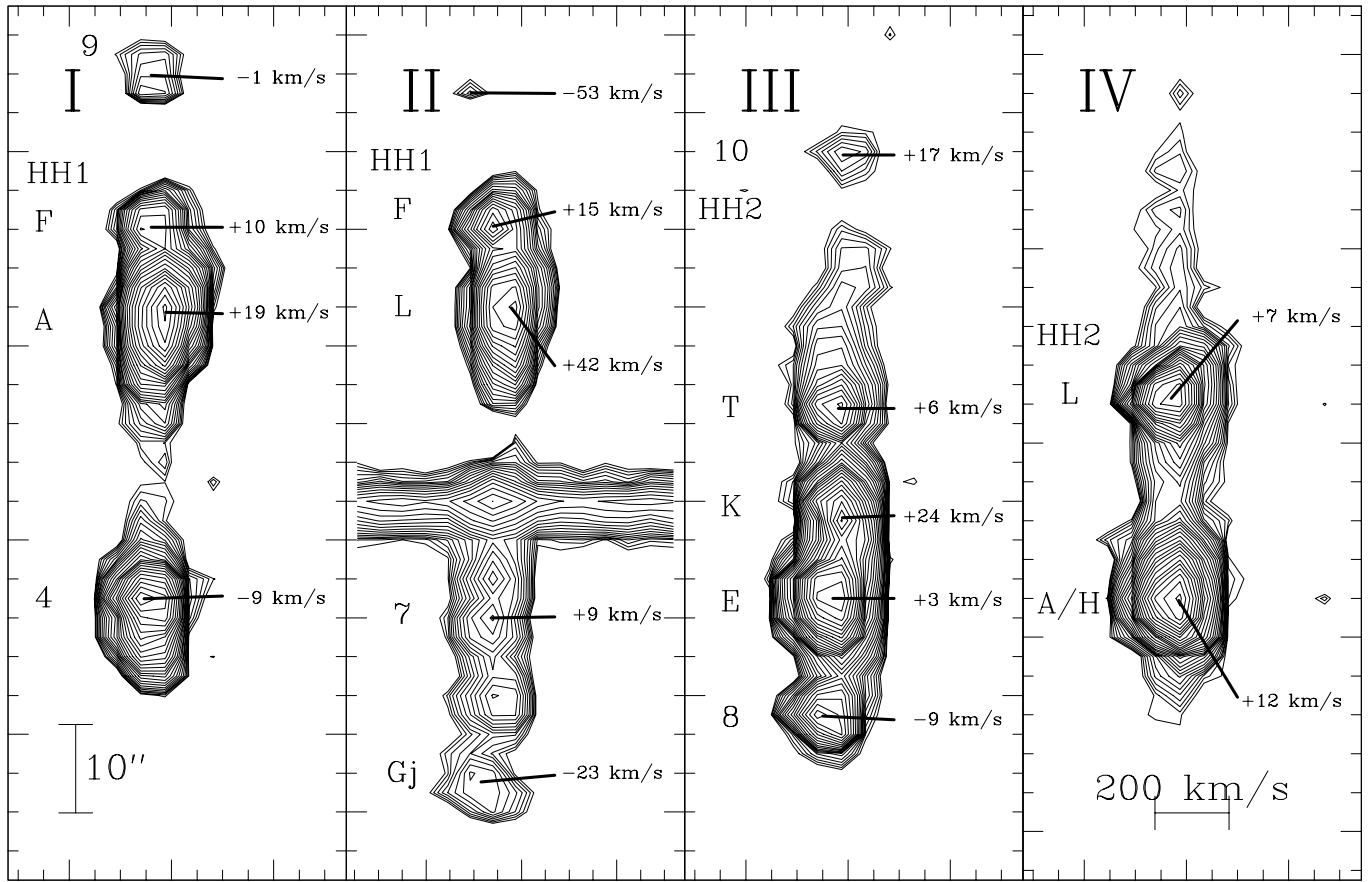


Fig. 3. Position-velocity diagrams towards HH 1/2 in the 1-0S(1) line of H₂ at 2.12 μm , in the slit positions marked in Fig. 2. Velocities are relative to a systemic velocity of HH 1/2 of $v_{l,SR} = 10.6 \text{ km s}^{-1}$ (Choi & Zhou 1997).

in our spectra. Knot 9 is situated ahead of the apex HH 1F of the HH 1 bow shock. In this region Solf & Böhm (1991) observed dust-scattered Herbig-Haro emission from the HH 1 jet in the optical atomic lines. Knot 10 is located in the heavily obscured region between HH 2 and the VLA1 source.

4.1.1. Radial velocities and H₂ line fluxes in HH 1/2

Our longslit spectra of HH 1 and HH 2 are presented in Fig. 3. One slit was centred on the HH 1 jet and bow shock, and a second one on the bright knots south-east of the Cohen & Schwartz star. Another two slits cross the HH 2 bow, covering its brightest H₂ condensations. Slit positions are numbered with roman numerals as in Fig. 2. Designations of the brighter knots are indicated to the left of the spectra. Their corresponding radial velocities are given to the right. These radial velocities are relative to the systemic velocity of the HH 1/2 system of $v_{l,SR} = 10.6 \text{ km s}^{-1}$ (Choi & Zhou 1997). They should be accurate to about $\pm 10 \text{ km s}^{-1}$.

Measured line fluxes and upper limits for 11 ro-vibrational H₂ transitions in the K-band for various knots in HH 1 and HH 2 are listed in Table 2. They are ordered as the knots appear in the position-velocity diagrams I–IV in Fig. 3. Fluxes are in units of

$10^{-18} \text{ W m}^{-2}$, and individual measurement errors are given in brackets.

For most knots in HH 1 and 2, the radial velocities scatter by about 20 km s^{-1} around the systemic velocity. This is consistent with the radial velocities found in optical lines (e.g., Böhm & Solf 1985, 1992), and suggests that the HH 1/2 outflow is very close to the plane of the sky.

In HH 1, knots A and L possess quite high redshifted speeds, suggesting they are generated in material accelerated away from the HH 1 bow and away from the line of sight, i.e. they are forming the receding wing in this rather asymmetric bow shock. Several components between HH 1 and HH 2 possess a range of radial speeds, suggesting complex outflow dynamics (e.g., precession, pulsation, or cavity backflow). In HH 2, we find that the line of knots K, E, and 8 is increasingly blueshifted with distance from the source (slit III), and knots A/H and L (slit IV) are following the same pattern. A similar pattern of increasing blueshift with distance across HH 2 has also been found in a recent CO millimeter study by Moro-Martín et al. (1999) which traces the relatively cold gas. These observations suggest that we are seeing a flow that impacts with a cloud positioned so as to deflect debris predominantly towards the observer.

Table 2. H₂ integrated line fluxes in HH 1/2.

line	3-2 S(5)	2-1 S(3)	1-0 S(1)	8-6 O(5)	1-0 S(0)	2-1 S(1)	9-7 O(3)	3-2 (S1)	1-0 Q(1)	1-0 Q(2)	1-0 Q(3)
knot	2.065 μ m	2.072 μ m	2.121 μ m	2.210 μ m	2.223 μ m	2.247 μ m	2.253 μ m	2.386 μ m	2.406 μ m	2.413 μ m	2.423 μ m
slit HH 1/2 I											
HH 1 knot 9	<5	3(4)	17(4)	2(3)	2(3)	4(4)	<6	6(6)	11(8)	7(8)	<10
HH 1 F	2(1)	5(4)	55(6)	3(4)	27(6)	14(5)	6(6)	8(5)	24(10)	16(5)	18(11)
HH 1 A	3(1)	54(8)	371(9)	1(2)	75(8)	55(5)	<9	12(10)	170(57)	89(21)	113(22)
HH 1 knot 4	5(4)	7(2)	224(11)	5(7)	40(13)	16(18)	<8	8(7)	218(28)	69(31)	91(6)
slit HH 1/2 II											
HH 1 F	<8	12(5)	99(5)	-	-	8(10)	<11	9(14)	159(39)	56(42)	74(61)
HH 1 L	10(9)	32(9)	184(6)	-	-	13(9)	<9	2(10)	10(14)	50(15)	<25
HH 1 knot 7	2(2)	3(2)	43(6)	-	-	<4	<5	2(7)	7(8)	30(20)	<12
HH 1 G _j	<3	3(3)	5(1)	-	-	<3	<3	3(7)	6(11)	27(9)	13(8)
HH 1 G _j	<4	4(2)	20(2)	-	-	1(6)	<6	8(10)	48(21)	20(14)	15(21)
slit HH 1/2 III											
HH 2 knot 10	7(8)	4(9)	46(11)	7(6)	<8	3(4)	<9	7(6)	11(10)	10(15)	4(13)
HH 2 T	3(3)	7(6)	71(2)	2(3)	15(3)	4(2)	<5	5(3)	17(6)	6(9)	24(19)
HH 2 K	2(3)	19(5)	159(4)	7(2)	38(4)	9(3)	<5	3(4)	109(18)	31(4)	54(6)
HH 2 E	9(7)	57(2)	512(5)	4(6)	128(7)	39(4)	<5	8(7)	369(17)	137(15)	200(21)
HH 2 knot 8	2(2)	4(2)	74(5)	5(6)	34(3)	3(2)	<5	2(4)	67(9)	38(24)	22(26)
slit HH 1/2 IV											
HH 2 L	5(8)	37(10)	244(12)	5(7)	42(5)	18(5)	17(3)	12(12)	108(24)	35(14)	39(13)
HH 2 A/H	<8	47(11)	428(9)	7(6)	86(5)	19(3)	10(6)	9(13)	131(19)	36(11)	59(23)

^a Fluxes are in 10⁻¹⁸ W m⁻². Errors are given in brackets.

4.1.2. Excitation of H₂ in HH 1/2

The H₂ line fluxes listed in Table 2 are presented as CDR diagrams in Fig. 4 for the knots in HH 1/2 where the data are of sufficient quality. Straight line fits to log(CDR)-T_j are superimposed using the two most accurate lines, and the corresponding vibrational excitation temperatures are given. Extinctions, A, at 2.12 μ m are calculated from the 1-0 Q(3)/1-0 S(1) line ratio, where possible, and otherwise are assumed to be zero. Q-branch lines are represented by open squares (these columns, at wavelengths exceeding 2.4 μ m, i.e. towards the edge of the K-band atmospheric window, are less reliable). Upper limits are shown as crosses with arrows.

We find from these diagrams that HH 1 presents a very cool H₂ knot F at the apex of the bow. This cool gas is explained by a new H₂ image which shows that this knot is a highly-oblique, almost planar shock segment (Davis et al. 2000). The wings HH 1A and L are relatively warm, \sim 2500 K, an excitation often found in outflows (Burton et al. 1989; Gredel 1994, 1996). Close to the source, a trend for sharply falling excitation with distance from the source is seen along the HH 1 jet (knots HH 1G_j and 7). This is consistent with the new H₂ and [FeII] images of Davis et al. (2000) and Reipurth et al. (2000), since both groups find a decreasing [FeII]/H₂ ratio with distance downwind.

The northern side of HH 2 presents three well-observed knots in which the excitation becomes progressively weaker with distance from the source (knots HH 2K, E, and knot 8). This may be consistent with a general trend for lower excitation with distance from the outflow source in HH 1/2, as well as in the HH 46/47 outflow discussed below (see for example

condensations HH 46 knots 1/2/3 and HH 47C counterjet knots a and b).

A fluorescent signature is possibly found in knots HH 2A/H and L. Especially in HH 2A/H, we find both the 8-6 O(5) and 9-7 O(3) vibrational transitions may be present at a marginal level. In comparison, the Black & van Dishoeck (1987) model predicts that the 1-0 S(1) and 2-1 S(1) contributed fluxes should be \sim 10 and \sim 5 times larger than the 9-7 O(3) flux. Instead, the observed 2-1 S(1) flux is a factor of 3 lower than this prediction. Thermalisation, within a high density molecular gas, in which the 2-1 S(1) upper energy level becomes collisionally (rather than radiatively) depopulated could reduce the required flux. Densities would then have to far exceed 10⁶ cm⁻³, though. A second problem is the high ratio of 1-0 S(1)/1-0 S(0) of 5.0 \pm 0.4: other photon-dominated regions possess ortho-para ratios lower than 3. This is not clear evidence, since we do not know the rotational excitation from just the two 1-0 lines, but given that the 1-0 S(2) flux must be high to yield a low ortho-para ratio, the resulting rotational temperature would exceed by far the vibrational temperature, and the model is thus inconsistent. Clearly, better data, including the 1-0 S(2) line would aid the interpretation. Note also that knot HH 2A/H corresponds to Böhm & Solf's (1985) atomic high excitation knot, for which they found strange velocity dispersion properties.

Our derived K-band extinction values are all close to or consistent with zero, in as far as one trusts the 1-0 Q(3) flux. This means that there is little extinction in front of and within the measured knots in HH 1/2.

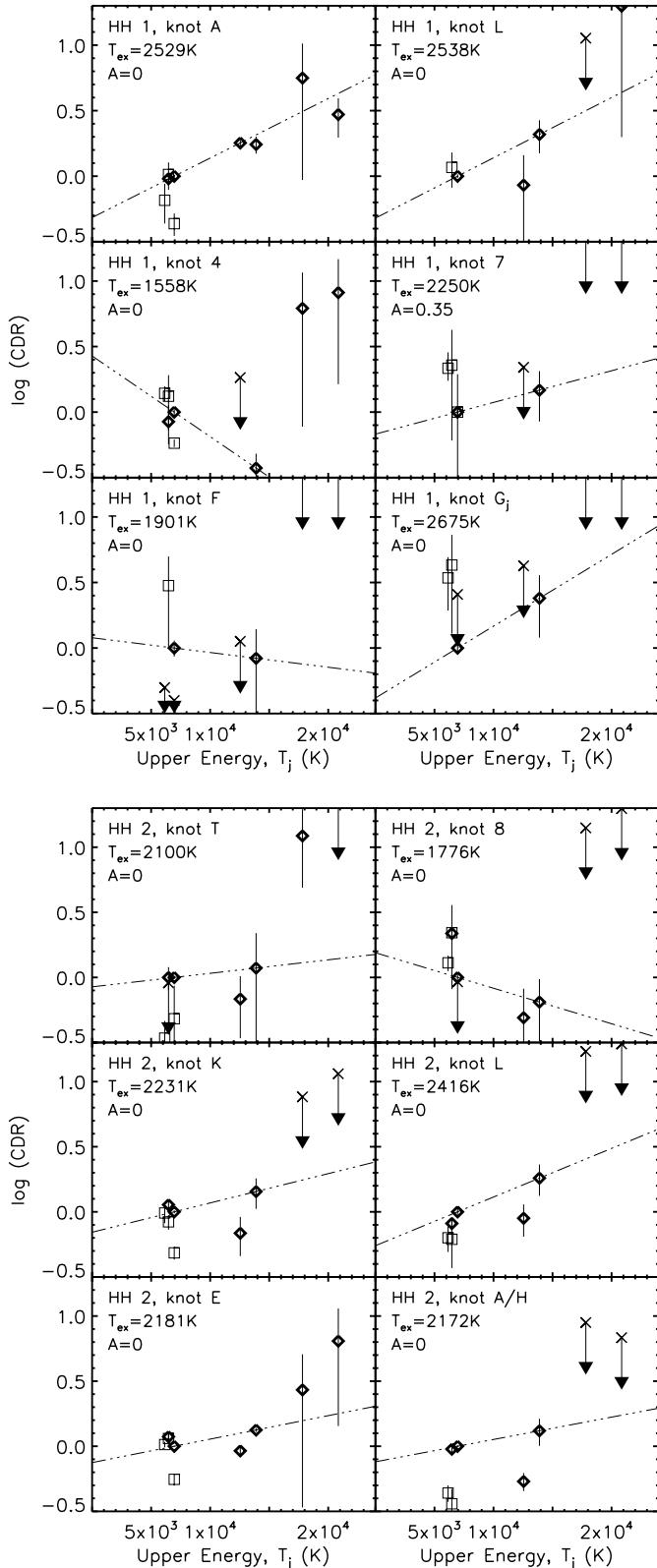


Fig. 4. H₂ CDR diagrams for selected regions within HH 1/2. Straight line fits to $\log(\text{CDR})-T_j$ are superimposed using the two most accurate lines. Corresponding vibrational excitation temperatures and extinctions, A , at $2.12\mu\text{m}$ are given. Q-branch lines are represented by open squares, and upper limits are shown as crosses with arrows.

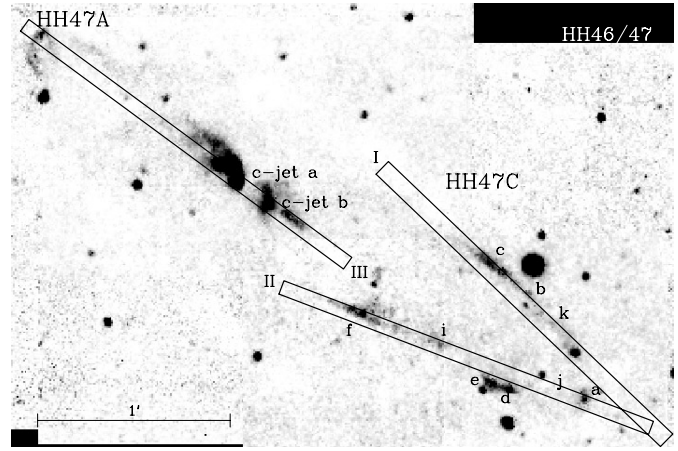


Fig. 5. Observed slit positions in HH 46/47 on an image in the 1-0S(1) line of H₂ at $2.12\mu\text{m}$. Roman numerals indicate the end of the slits that appear at the top in Fig. 6.

4.2. HH 46/47

HH 46/47 was imaged in the near-infrared 1-0S(1) line of H₂ and in the [FeII]1.64 μm by Eisloffel et al. (1994). They interpreted the H₂ emission stretching backwards along the northern side of the north-eastern HH 46/47 jet, and from the south-western HH 47C bow towards the source as the wings of extended bow shocks. Proper motions in H₂ for some of the knots in these wings, as well as in the HH 47 counterjet were measured by Micono et al. (1998).

An image of the HH 46/47 outflow in the 1-0S(1) line of H₂ at $2.12\mu\text{m}$ is presented in Fig. 5. The positions of our three IRSPEC longslits are indicated. Three fainter knots in the wings of the HH 47C bow, which we can clearly identify in our spectra, are marked i, j, k in continuation of the numbering scheme of Micono et al. (1998).

4.2.1. Radial velocities and H₂ line fluxes in HH 46/47

Our IRSPEC longslit spectra of HH 46/47 are presented in Fig. 6. Two slits were positioned on the emission features in the wings of the HH 47C bow, while another slit was centred on the flow axis, covering both the jet and the counterjet. Slit positions are numbered with roman numerals as in Fig. 5. Designations of the brighter knots are indicated to the left of the spectra. Their corresponding radial velocities are given to the right. These radial velocities are relative to the systemic velocity of the HH 46/47 system of $v_{lsr} = 5.5\text{ km s}^{-1}$ (Olberg et al. 1992). They should be accurate to about $\pm 10\text{ km s}^{-1}$.

Measured line fluxes and upper limits for 12 ro-vibrational H₂ transitions in the K-band for various knots in HH 46/47 are listed in Table 3. They are ordered as the knots appear in the position-velocity diagrams I–III in Fig. 6.

High redshifted radial velocities of about $+50\text{ km s}^{-1}$ are measured at and near the apex of the HH 47C bow (knot a). They are diminishing continuously along the flanks of the partial shell (slits I and II), and even get negative in knots i and f. This is

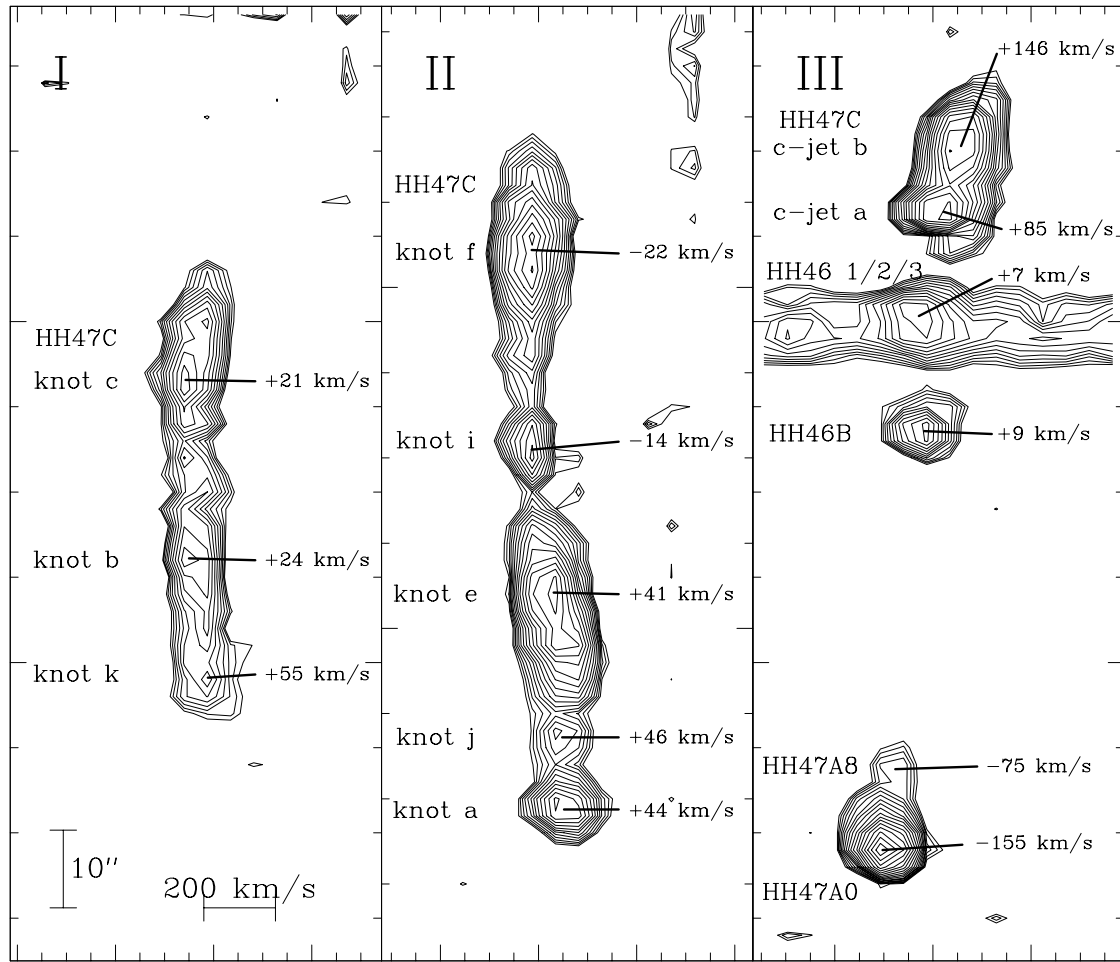


Fig. 6. Position-velocity diagrams towards HH 46/47 in the 1-0 S(1) line of H₂ at 2.12 μm , in the slit positions marked in Fig. 5. Velocities are relative to a systemic velocity of HH 46/47 of $v_{lsr} = 5.5 \text{ km s}^{-1}$ (Olberg et al. 1992).

Table 3. H₂ integrated line fluxes in HH 46/47

line	3-2 S(5)	2-1 S(3)	1-0 S(1)	3-2 S(4)	8-6 O(5)	1-0 S(0)	2-1 S(1)	9-7 O(3)	3-2 S(1)	1-0 Q(1)	1-0 Q(2)	1-0 Q(3)
knot	2.065 μm	2.072 μm	2.121 μm	2.127 μm	2.210 μm	2.223 μm	2.247 μm	2.253 μm	2.386 μm	2.406 μm	2.413 μm	2.423 μm
slit HH 46/47 I												
HH 47 C knot c	6(9)	28(6)	144(6)	-	<6	<6	34(7)	10(7)	2(7)	114(23)	<18	119(12)
HH 47 C knot b	7(9)	47(7)	110(6)	-	<7	5(5)	30(7)	<6	4(5)	78(13)	20(18)	82(13)
HH 47 C knot k	2(5)	6(6)	30(9)	-	<5	2(5)	<5	<6	1(7)	25(12)	<15	32(10)
slit HH 46/47 II												
HH 47 C knot f	3(3)	17(18)	83(46)	9(6)	8(9)	8(11)	5(7)	<9	17(22)	91(60)	30(20)	33(26)
HH 47 C knot i	6(7)	8(8)	23(13)	3(3)	5(5)	6(6)	3(2)	<4	8(10)	25(28)	5(5)	13(7)
HH 47 C knot e	10(10)	15(9)	133(27)	5(6)	11(12)	29(26)	15(7)	<7	4(7)	88(15)	29(8)	72(36)
HH 47 C knot j	3(3)	3(4)	15(7)	3(2)	2(5)	2(2)	1(3)	<4	3(6)	7(7)	7(6)	21(16)
HH 47 C knot a	5(5)	5(5)	29(9)	1(2)	<5	3(3)	<4	<4	1(1)	22(14)	12(15)	28(20)
slit HH 46/47 III												
HH 47 c-jet b	1(1)	9(6)	75(4)	-	6(7)	16(13)	<4	<5	5(5)	35(18)	16(11)	59(15)
HH 47 c-jet a	2(4)	8(7)	59(13)	-	6(7)	16(8)	9(9)	<5	2(3)	31(11)	20(11)	27(12)
HH 46 1/2/3	1(1)	11(6)	20(5)	-	5(6)	6(3)	<5	<5	3(6)	20(10)	7(2)	13(7)
HH 46 B	3(4)	6(5)	25(4)	-	2(3)	10(3)	5(4)	<5	<8	17(10)	3(6)	13(12)
HH 47 A ₈	3(4)	4(8)	21(8)	-	1(2)	8(4)	5(4)	4(3)	1(3)	7(11)	5(7)	14(5)
HH 47 A ₀	6(7)	15(7)	59(10)	-	9(10)	13(4)	15(7)	3(3)	4(6)	30(8)	21(17)	37(13)

^a Fluxes are in $10^{-18} \text{ W m}^{-2}$. Errors are given in brackets.

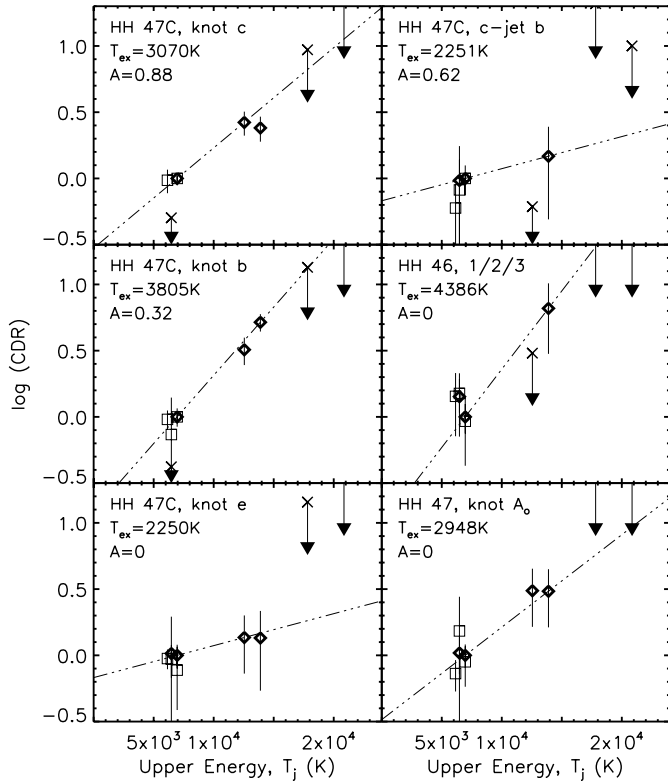


Fig. 7. H_2 CDR diagrams for selected regions within HH 46/47. See also caption to Fig. 4.

consistent with a partial bow model, rather than a wind-blown cavity in which the wind is focussed. Even higher redshifted velocities of up to $+145 \text{ km s}^{-1}$, and a strong increase in the radial velocity of the H_2 gas with distance from the source, are observed in the counterjet (slit III). A similar increase, up to a blueshifted radial velocity of -155 km s^{-1} , is also seen in the northeastern HH 46/47 jet (HH 46B – 47A). Indeed, slit III illustrates the striking radial velocity gradient between the jet and counterjet in HH 46/47. The radial velocity increases with distance from the source may be due to variations in the jet speed. Numerical hydrodynamic simulations of pulsed jets indeed show such a behaviour in the H_2 emission from the inner jet (see Fig. 14 of Völker et al. 1999).

4.2.2. Excitation of H_2 in HH 46/47

The H_2 line fluxes listed in Table 3 are presented as CDR diagrams in Fig. 7 for the knots in HH 46/47 for which the data warrant further analysis. We find that the individual knots b and c in the northern flank of the partial H_2 bow HH 47C are of high excitation, consistent with J-type shock models JSLOW and JBOW. The CSHOCK model cannot be excluded with the present data, but requires very specific and uniform conditions. The extinction along the northern edge of the counter-flow shell (knots b and c) appears to be quite high. This may be related to the redshifted motions, suggesting a high internal extinction, which also hides any optical emission from this lobe. The south-

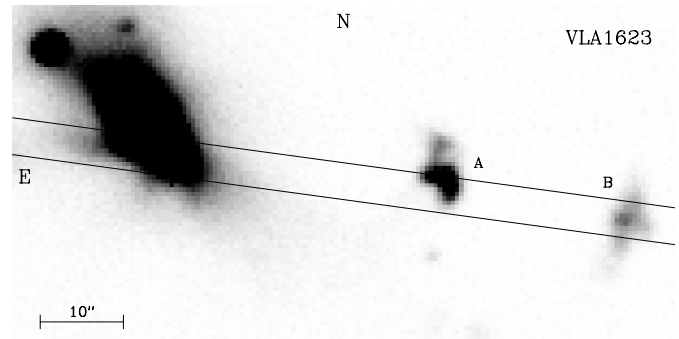


Fig. 8. Observed slit position in VLA 1623 on an image in the 1-0 S(1) line of H_2 at $2.12 \mu\text{m}$. Knots A and B from Davis & Eisloffel (1995) have been marked.

ern edge of the shell is cooler with lower extinction, consistent with the blueshifted velocity, indicating motion towards the observer. Given an angle to the line of sight of 62° , and the apparently wide cavity, this material may be breaking through the near side of the Bok globule. Knots b and c in the northern flank of the bow would appear to have an extreme ortho:para ratio (with both para lines being undetected in knot c). These strange results could be a measure of the ortho:para ratio within the cold Bok globule. In a cold low density medium in which only the ground states of ortho- and para- H_2 are occupied, thermal equilibrium would eventually produce an ortho:para ratio of 9. Consequent excitation, without time to reduce the modification ratio, could then produce the observed result.

The counter jet is quite cool, just over 2000 K. We derive an extinction towards c-jet knot b of 0.62 magnitudes, or about 6 magnitudes in the optical. The bow HH 47A of the HH 46/47 jet has a high blueshift of -155 km s^{-1} , and a high excitation of $\sim 3000 \text{ K}$. This speed is consistent with the atomic emission line velocity images (Hartigan et al. 1993), favouring emission from the bow shock rather than the Mach disk.

4.3. VLA 1623

The outflow from VLA 1623 was imaged in the 1-0 S(1) line of H_2 by Davis & Eisloffel (1995) and Dent et al. (1995). Both low- and high-resolution spectroscopy of VLA 1623A led Davis et al. (1999) to conclude that this object is a C-type bow moving towards the observer at an angle to the line of sight of $\sim 75^\circ$ at a speed of $\sim 80 \text{ km s}^{-1}$.

An image of knots A and B in the VLA 1623 outflow in the 1-0 S(1) line of H_2 at $2.12 \mu\text{m}$ is shown in Fig. 8. To the left, the bright reflection nebula of the class I source GSS30 is seen (see also Dent et al. 1995). Two solid lines mark the position of our IRSPEC longslit, which was centred on the two emission knots and the GSS30 source.

4.3.1. Radial velocities and H_2 line fluxes in VLA 1623

A position-velocity diagram towards VLA 1623 A and B in the 1-0 S(1) line of H_2 at $2.12 \mu\text{m}$ from our IRSPEC longslit spec-

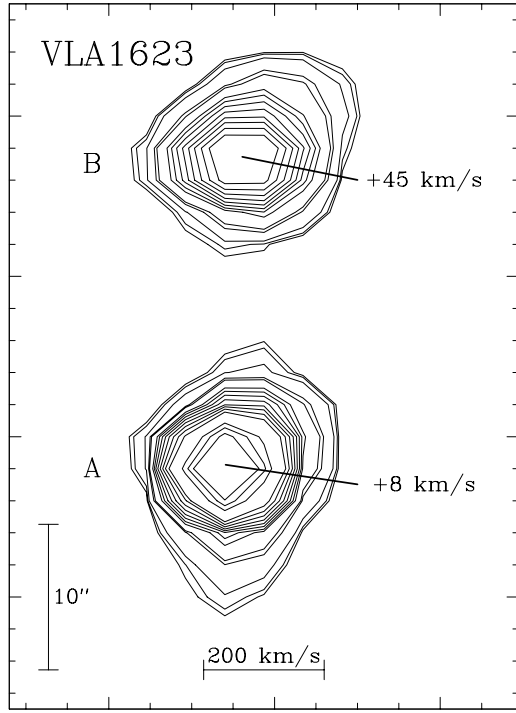


Fig. 9. Position-velocity diagram towards VLA 1623 in the 1-0S(1) line of H₂ at 2.12 μm , in the slit positions marked in Fig. 8. Velocities are relative to a systemic velocity of VLA 1623 of $v_{LSR} = 3.8 \text{ km s}^{-1}$ (André et al. 1990).

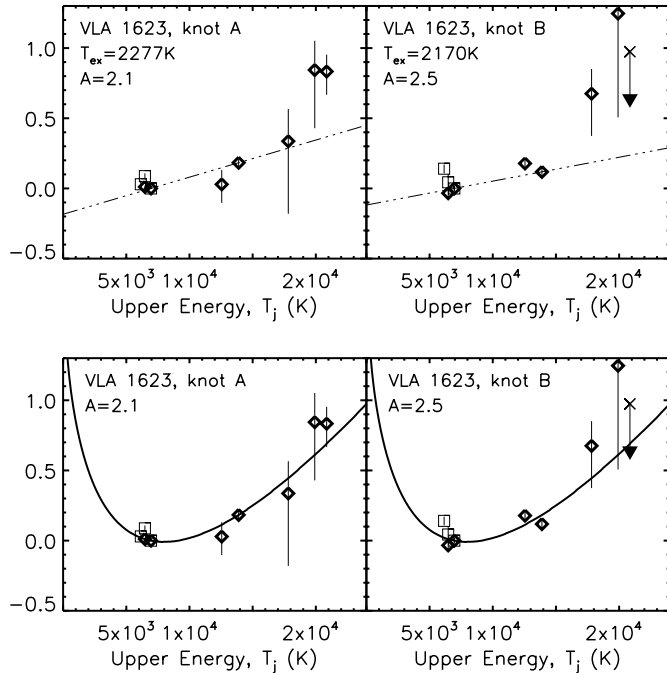


Fig. 10. Upper panel: H₂ log(CDR) diagrams for regions within VLA 1623, with straight line fits to log(CDR)- T_j superimposed using the two most accurate lines. See also caption to Fig. 4. Lower panel: The C-type bow shock model successfully employed to interpret the UKIRT CGS4 spectra Davis et al. (1999) for locations within knot A is here used to compare with the H₂ log(CDR) diagrams for the VLA 1623 knots. See the text for the model parameters.

Table 4. H₂ integrated line fluxes in VLA 1623

line	wavelength	A	B
3-2 S(5)	2.065 μm	22(7)	5(5)
2-1 S(3)	2.072 μm	152(9)	43(4)
1-0 S(1)	2.121 μm	1292(10)	432(13)
3-2 S(4)	2.127 μm	13(8)	11(9)
8-6 O(5)	2.210 μm	<4	1(2)
1-0 S(0)	2.223 μm	325(7)	101(9)
2-1 S(1)	2.247 μm	137(36)	67(5)
9-7 O(3)	2.253 μm	7(12)	5(7)
3-2 S(1)	2.386 μm	23(16)	18(9)
1-0 Q(1)	2.406 μm	1409(88)	655(46)
1-0 Q(2)	2.413 μm	540(26)	176(24)
1-0 Q(3)	2.423 μm	1343(121)	486(24)

^a Fluxes are in $10^{-18} \text{ W m}^{-2}$. Errors are given in brackets.

trum is shown in Fig. 9. A small redshifted radial velocity of $+8 \text{ km s}^{-1}$, relative to the systemic velocity of $v_{LSR} = 3.8 \text{ km s}^{-1}$ (André et al. 1990), is measured here for knot A, although Davis et al. (1999) find a small blueshifted radial velocity of about -6.5 km s^{-1} for the part of knot A common to both measurements. Given our measurement error of about $\pm 10 \text{ km s}^{-1}$, however, and the fact that Davis et al. (1999) suggest part of knot A (not covered by their slits) may actually belong to a different outflow, the two measurements are not contradictory. Also knot B, for which we find a radial velocity of $+45 \text{ km s}^{-1}$, may be related to this second flow with a source perhaps in the nebula GSS 30. Proper motions within knot A and between knots A and B will eventually clarify the situation.

Measured H₂ line fluxes and upper limits for knots VLA1623 A and B in 12 ro-vibrational H₂ lines in the K-band are listed in Table 4.

4.3.2. Excitation of H₂ in VLA 1623

The H₂ line fluxes listed in Table 4 are presented as CDR diagrams in Fig. 10. We find that the infrared K-band extinction in this flow is rather high at 2–3 magnitudes. This is consistent with the result from the spectroscopy of Davis et al. (1999), where the extinction across knot A was found to systematically increase from 2 to 3 magnitudes.

We can dismiss the CSHOCK and 1TEMP models immediately for the knots of the VLA 1623 flow for the following reason. While the H₂ excitation temperatures as measured from the 2-1 S(1)/1-0 S(1) line ratio are just over 2000 K, the detection of several 3-2 lines imply that a single temperature model (CSHOCK or 1TEMP) is not relevant.

Bow shocks are clearly involved for both knots, as was concluded for knot A by Davis et al. (1999). The two knots possess very similar excitation properties, consistent with the predictions of bow shock models which combine bow zones of hot, warm and cool gas in amounts prescribed mainly by the bow shape. In fact, we find remarkably accurate fits for both knots by employing exactly the model which was so successful in the interpretation of the longslit spectroscopy of Davis et al.

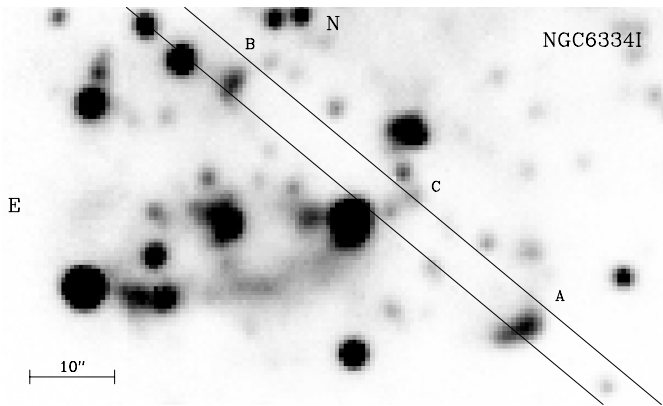


Fig. 11. Observed slit position in NGC 6334I drawn on an image in the 1-0 S(1) line of H₂ at 2.12 μm. Knots A, B, C from Davis & Eislöffel (1995) have been marked.

(1999), confirming this result. Fig. 10 demonstrates that the C-type paraboloidal bow shock of speed 80 km s⁻¹ moving at 75° to the line of sight, with a magnetic field at 45° to the flow axis, an Alfvén speed of 2 km s⁻¹, an ion fraction of 10⁻⁷, and O and CO abundances of 10⁻⁴ provides an excellent fit not only to the spatially-resolved excitation study and the position-velocity diagrams (Davis et al. 1999) but also to the integrated emission from the knots shown here. Note that only the oxygen abundance (through conversion into the critical coolant H₂O in the shock front) and the bow shape have a significant bearing on the excitation in a fast C-type bow (Smith et al. 1991a, 1991b).

4.4. NGC 6334I

An image of the central part of the NGC 6334I cluster in the 1-0 S(1) line of H₂ is shown in Fig. 11. The three H₂ emission knots A, B, C identified by Davis & Eislöffel (1995) are marked. The position of our IRSPEC longslit covering these three knots is indicated.

4.4.1. Radial velocities and H₂ line fluxes in NGC 6334I

A position-velocity diagram towards NGC 6334I covering the 1-0 S(1) line of H₂ at 2.12 μm in our IRSPEC longslit spectrum is shown in Fig. 12. The bipolar nature of the outflow is clearly indicated. Its blueshifted lobe towards the southwest is traced by knots A and C, which move at radial velocities of -18 km s⁻¹ and -20 km s⁻¹ relative to the systemic velocity of $v_{lsr} = -7.5 \text{ km s}^{-1}$ (Bachiller & Cernicharo 1990), while its redshifted lobe towards the northeast, which in H₂ consists of knot B, is moving at a radial velocity of +79 km s⁻¹ relative to the systemic velocity. It is surprising that knot C has almost the same blueshifted radial velocity as knot A. This implies that knots A and C are in the same lobe of the bipolar flow, and that the flow source is located somewhere between knots B and C. In fact, this casts some doubt on the previous suggestion that the far-infrared source IRS1 (Harvey & Gatley 1983), which

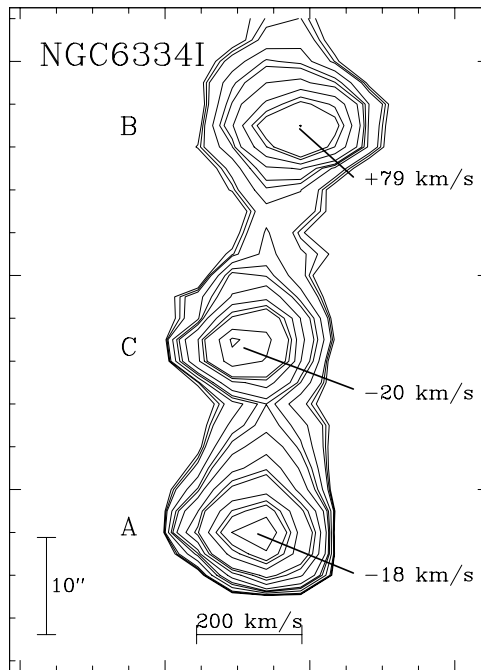


Fig. 12. Position-velocity diagram towards NGC 6334I in the 1-0 S(1) line of H₂ at 2.12 μm in the slit positions marked in Fig. 11. Velocities are relative to a systemic velocity of NGC 6334I of $v_{lsr} = -7.5 \text{ km s}^{-1}$ (Bachiller & Cernicharo 1990).

Table 5. H₂ integrated line fluxes in NGC 6334I

line	wavelength	A	B	C
3-2 S(5)	2.065 μm	12(7)	6(6)	11(7)
2-1 S(3)	2.072 μm	63(13)	24(14)	38(13)
1-0 S(1)	2.121 μm	551(16)	231(18)	297(21)
3-2 S(4)	2.127 μm	11(6)	7(4)	11(6)
8-6 O(5)	2.210 μm	<8	<5	<10
1-0 S(0)	2.223 μm	153(11)	72(6)	46(12)
2-1 S(1)	2.247 μm	52(9)	15(14)	24(9)
9-7 O(3)	2.253 μm	<7	<9	<9
3-2 S(1)	2.386 μm	26(25)	15(7)	24(13)
1-0 Q(1)	2.406 μm	719(39)	318(27)	342(53)
1-0 Q(2)	2.413 μm	234(14)	94(28)	98(37)
1-0 Q(3)	2.423 μm	681(27)	300(18)	230(48)

^a Fluxes are in 10⁻¹⁸ W m⁻². Errors are given in brackets.

coincides with the bright source ~5'' southeast of knot C, is the driving source of this flow (Davis & Eislöffel 1995).

Measured line fluxes and upper limits for the three observed knots NGC 6334I A, B, C in 12 ro-vibrational H₂ lines in the K-band are listed in Table 5. The two lines that have not been detected, and for which 1-σ upper limits are given, are the 8-6 O(5) and the 9-7 O(3) transitions.

4.4.2. Excitation of H₂ in NGC 6334I

The H₂ line fluxes listed in Table 5 are presented as CDR diagrams in Fig. 13. There, the H₂ excitation appears similar to

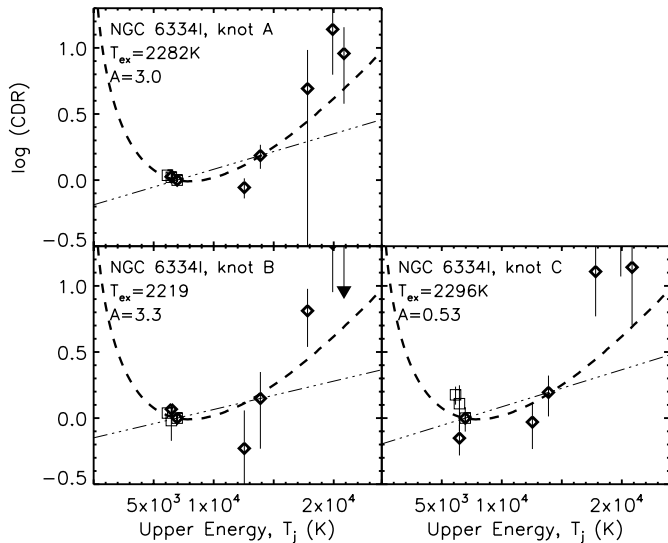


Fig. 13. H₂ CDR diagrams for regions within NGC 6334I with the C-type bow shock model (dashed line) as applied to VLA 1623 superimposed. The straight (dot-dashed) lines correspond to the excitation temperatures.

VLA 1623. Thus we display the same bow shock model for all three knots. For knots B and C, the third vibrational level appears to exceed the bow shock model predictions. In particular, the observed columns which produce the 3-2 S(1) line from $T_j = 17818$ K and the 3-2 S(4) line at 19912 K are high. This could indicate that a fluorescent component is present, especially in knot C.

Alternatively, the high ratio of 2-1 S(3) to 2-1 S(1) in all three knots (note, however, the errors in knots B and C) are consistent with a jump shock with speeds in the range 10–22 km s⁻¹. Smith (1995) found a ratio of 1.3 for this line ratio for model JSLOW. Then, the detected 3-2 lines would be explained by the same JSLOW model: it predicts the 3-2 S(5) line to be about 0.2 of the adjacent 2-1 S(3) line, as indeed observed. The 1-0 emission must then arise from cool gas, less than ~1500 K, or from somewhat warmer low density gas, with little collisional excitation above the first vibrational level. Given the obvious bow shock morphology of the knots in NGC 6334I, the “planar” JSLOW model is perhaps less likely than the CBOW (with fluorescence) interpretation. Nevertheless, further observations, especially at longer infrared wavelengths, are needed to test this scenario.

4.5. HH 57

4.5.1. Radial velocities and H₂ line fluxes in HH 57

A position-velocity diagram of HH 57 from our IRSPEC longslit spectrum covering the 1-0 S(1) line of H₂ at 2.12 μm is shown in Fig. 14. The central continuum spectrum belongs to the FU Orionis object V346 Nor, the source of the HH 57 outflow. This outflow manifests itself in the blueshifted knot A and the redshifted knot HH 57B in the counterflow, which is detected here for the first time. The radial velocities of these knots A and B are mea-

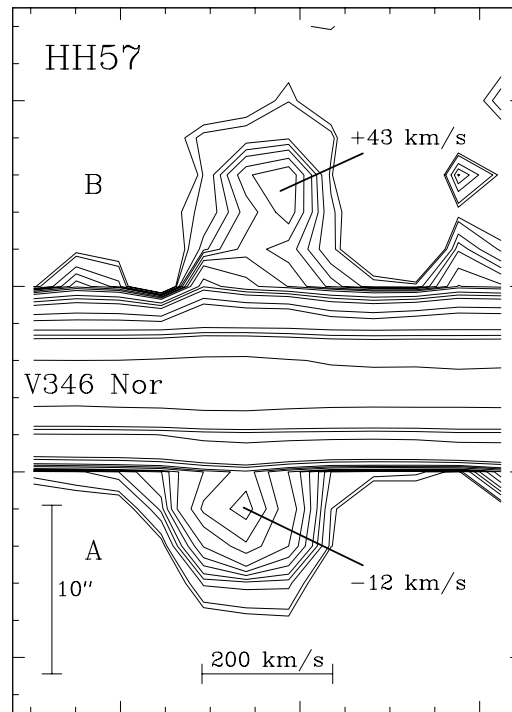


Fig. 14. Position-velocity diagram towards HH 57 in the 1-0 S(1) line of H₂ at 2.12 μm. Emission from the counterflow (knot B) is clearly visible. Velocities are relative to a systemic velocity of HH 57 of $v_{lsr} = -3.1$ km s⁻¹ (Evans et al. 1994).

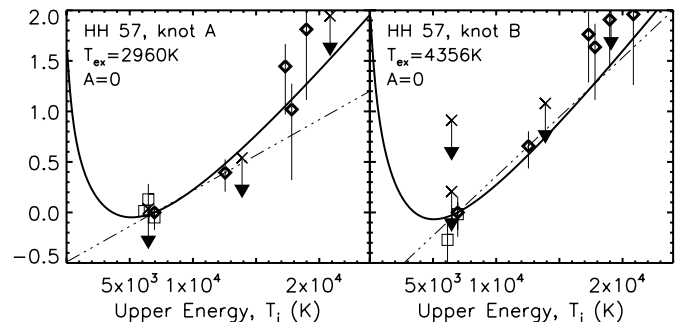


Fig. 15. H₂ CDR diagrams for regions within HH 57. See also caption to Fig. 4. The dot-dash is a single temperature fit to the strongest pair of lines. The solid lines are from JSLOW models with a shock speed of 15 km s⁻¹, an oxygen abundance of $4 \cdot 10^{-4}$ and a pre-shock hydrogen nucleon density of 10^5 cm⁻³ (left) and 10^4 cm⁻³ (right).

sured as -12 km s⁻¹ and $+43$ km s⁻¹ relative to the systemic velocity of $v_{lsr} = -3.1$ km s⁻¹ (Evans et al. 1994). Measured line fluxes and upper limits of these knots in the [FeII]λ1.64 μm line and in 13 ro-vibrational lines of H₂ throughout the H- and K-band are given in Table 6.

4.5.2. Excitation of H₂ in HH 57

The H₂ line fluxes listed in Table 6 are presented as CDR diagrams in Fig. 15. We find that the H₂ excitation temperatures are very high in HH 57. Hence the C-type bow shock model fails to explain the observed H₂ here. On the other hand, the 1-

Table 6. H₂ integrated line fluxes in HH 57

line	wavelength	A	B
[Fe II]	1.644 μm	37(17)	5(6)
1-0 S(11)	1.650 μm	10(8)	6(4)
1-0 S(10)	1.666 μm	6(4)	6(4)
3-2 S(5)	2.065 μm	8(12)	10(8)
2-1 S(3)	2.072 μm	10(14)	20(20)
1-0 S(1)	2.121 μm	83(14)	40(17)
8-6 O(5)	2.210 μm	5(7)	5(63)
1-0 S(0)	2.223 μm	8(11)	12(57)
2-1 S(1)	2.247 μm	17(6)	15(6)
9-7 O(3)	2.253 μm	<6	<14
3-2 S(1)	2.386 μm	5(4)	10(7)
1-0 Q(1)	2.406 μm	60(7)	15(8)
1-0 Q(2)	2.413 μm	26(11)	6(9)
1-0 Q(3)	2.423 μm	52(13)	27(8)

^a Fluxes are in $10^{-18} \text{ W m}^{-2}$. Errors are given in brackets.

0 S(1)/2-1 S(1) ratio is ~ 3 –5, which is within the standard range predicted by the JSLOW model (Smith 1995).

There is no evidence for extinction in the knots despite the high optical extinction to the central star. This suggests that a compact envelope surrounds the star and the outflow has broken out of this envelope on both sides.

Model JSLOW fits are shown in Fig. 15. The JSLOW model predictions are not sensitive to the oxygen abundance when above 0.5×10^{-4} , transverse magnetic fields which yield Alfvén speeds less than $\sim 6 \text{ km s}^{-1}$ or shock speeds in the range 10–22 km s^{-1} . Note, however, the density dependence which we have utilised to model the difference in excitation between the two knots (hot gas in the higher density shock is cooled more efficiently by water).

Note also that the emission from the [FeII] $\lambda 1.64 \mu\text{m}$ line may *not* originate from these shocks: Smith (1994) calculated that, for JSLOW models, this line flux is less than ~ 0.03 of the 1-0 S(1) flux. This suggests that the [FeII] is produced by the faster shocks, JFAST, which produce the optical Herbig-Haro object but relatively little H₂ emission.

JBOW models predict considerably less excitation than observed (see Smith 1994). Fluorescent models, FLO and FLY, are also not likely to be relevant since the detections of the 1-0 S(10) and S(11) lines confirms the thermal excitation of the hot gas. These two lines would not be detected here if fluorescence dominated.

5. Discussion

5.1. Excitation models

The CDR diagrams presented in the previous sections provide information about the shock physics and geometry. From our longslit spectroscopy we have found that the excitation is not constant, but in some objects is strongly dependent on the location within the outflow. The distribution of the excitation of H₂ within the outflows is consistent with the shock shape: oblique shocks (HH 1, knot F) and bow shocks (e.g., VLA 1623) pro-

vide explanations which are consistent with the images. These data are consistent with C-type shock physics. J-type molecular shocks are favoured in specific objects, such as HH 57, where an on-going FU-Orionis type outburst may be responsible for high ionisation levels. On the other hand, we find no evidence in the large lobe of HH 46/47 for a systematic trend on large scales. Instead, this means that we may be observing fragments of a broken cavity structure here, excited by outward propagating shocks, rather than a smooth shell in which we see the shell surfaces which are projected edge-on to the observer. Also, the large HH 1 bow structure consists of numerous mini bow shocks. Thus oblique edges appear even near the front of the overall structure, consistent with the HST optical images (Hester et al. 1998).

Gradients in H₂ velocity and excitation across HH 2 have been uncovered. The velocity and the excitation of the H₂ gas both decrease downstream towards the southeast, along with the atomic excitation and the CO velocity (Moro-Martin et al. 1999). This is evidence for the decay of supersonic turbulence in the wake of the proposed jet-cloud impact at knot A/H in HH 2 (Hester et al. 1998). The low molecular vibrational excitation displayed in knot 8, however, may also be explained by a low density in this region which, through the lack of compensating collisions, causes the second vibrational level to be radiatively depopulated.

5.2. The leading H₂ knots in the HH 1 and HH 47C bows

In previous imaging studies compact molecular hydrogen knots have been observed at the tips of the bow structures in HH 1 and HH 47C. The question arose why the H₂ molecules can survive in these places of highest shock speeds without being dissociated, and how they would be excited there. Here, we find that the excitation, radial velocity and resolved shape of the HH 1 tip are all consistent with this being an oblique shock on a leading mini-bow shock. Such leading mini-bows with low radial speeds were also found in numerical simulations of molecular outflows (e.g., Völker et al. 1999). The excitation of the HH 47C tip (knot a) was not determined here, although the upper limit on the 2-1 S(1) emission (Table 3) implies a 1-0 S(1)/2-1 S(1) ratio exceeding 5, and thermal excitation rather than fluorescence. Thus, a particular shape seems to reduce the shock speeds so far in these knots, that dissociation of the molecules is not a dominant process here. Higher resolution near-infrared images of HH 47C are, needless to say, desirable.

5.3. Kinematics of the southwestern HH 47 counterjet

Two H₂ infrared knotty jets have been observed in the course of this work. Both the HH 1 and HH 47 jet knots decrease in excitation with distance from the source. The HH 47 jet displays a steeply increasing radial velocity gradient which would be consistent with the shocked fragments from an impulsive event. In fact, the radial velocities observed here of 85 and 146 km s^{-1} are proportional to the proper motion speeds derived by Micono et al. (1998) of 136 and 229 km s^{-1} for knots c-jet a and c-jet

b, respectively, to within the errors of about 20%. The radial velocity knots were separated by $\sim 9''$ and the proper motion knots by $\sim 11''$, in rough agreement. An angle to the line of sight of $58 \pm 12^\circ$ is inferred on assuming ballistic motions. This compares to an angle of 55° derived from optical data for the bow shocks, taking a distance of 350 pc (Eislöffel & Mundt 1994). From these velocity data and the distance to the source (see also Fig. 6) a kinematical age of about 280 years is derived for both knots, hinting at a major outbreak of the HH 46 IRS source at that time.

The decreasing excitation in jet knots is a general prediction for pulsed jets (Smith et al. 1997b). Pulses rapidly steepen into shocks, which then gradually weaken as jet material is swept up into the knots, leaving less and less un-shocked material available to enter the shocks. Thus the shock pressure falls and the knots fade. Smith et al. (1997b), however, analysed and simulated pulses superimposed on uniform jets. It is not clear that accelerating jets should also display this shock decay process.

6. Conclusions

We have used new medium-resolution longslit spectroscopy to examine the excitation of molecular hydrogen across the outflows from HH 1/2, HH 46/47, HH 57, VLA 1623, and NGC 6334I. In contrast to previous studies, in which the brightest patches in the flows were selected, we find evidence for variations in excitation with position within several of these flows.

We present and comment on a number of H₂ excitation mechanisms of outflows from the literature, and compare them with our observations: H₂ position-velocity diagrams for all objects and line fluxes support a picture in which the excitation variations are caused by the large-scale shock geometry. In general, the variations are best interpreted by magnetohydrodynamic C-shocks, although some locations which demonstrate hydrodynamic J-type excitation are found. In particular, VLA 1623 is accurately modelled by a C-type bow, whereas a planar J-type shock model is favoured for HH 57. HH 1/2, on the other hand, consists of a collection of molecular bow and planar shocks. Another interesting result in this object is the finding that the H₂ emission from the leading edge of the HH 1 bow structure is actually from a low-excitation oblique wing associated with one of many mini-bow shocks (the leading mini-bow, in fact) rather than from fluorescence or a magnetic precursor.

In two of our objects, HH 1 and HH 47C, the jets themselves are also traced in molecular hydrogen emission. Radial velocities in the infrared jet in HH 47C demonstrate an acceleration of the knots which is consistent with their proper motions. This hints at ballistic motions of these knots, originating in an eruptive event about 280 years ago. In this jet, as well as in the HH 1 infrared jet, we find the excitation to decline with distance from the source.

Acknowledgements. We would like to thank Roland Gredel and the La Silla infrared group for their support during the observations. We also thank Tom Ray for much time spent discussing jets and outflows.

References

- André P., Martin-Pintado J., Despois D., Montmerle T., 1990, *A&A* 236, 180
- Ayala S., Curiel S., Raga A.C., Noriega-Crespo A., Salas L., 1998, *A&A* 332, 1055
- Bachiller R., Cernicharo J., 1990, *A&A* 239, 276
- Black J.H., van Dishoeck E.F., 1987, *ApJ* 322, 412
- Böhm K.H., Solf J., 1985, *ApJ* 294, 533
- Böhm K.H., Solf J., 1992, *AJ* 104, 1193
- Brand P.W.J.L., Moorhouse A., Burton M.G., et al., 1988, *ApJ* 334, L103
- Burton M.G., Brand P.W.J., Geballe T.R., Webster A.S., 1989, *MNRAS* 236, 409
- Burton M.G., Haas M.R., 1997, *A&A* 327, 309
- Choi M., Zhou S., 1997, *ApJ* 477, 754
- Davis C.J., Smith M.D., Eislöffel J., 2000, *MNRAS*, in press
- Davis C.J., Eislöffel J., Ray T.P., 1994, *ApJ* 426, L93
- Davis C.J., Eislöffel J., 1995, *A&A*, 300, 851
- Davis C.J., Smith M.D., 1995, *ApJ* 443, L41
- Davis C.J., Smith M.D., 1996, *A&A* 310, 961
- Davis C.J., Smith M.D., Eislöffel J., Davies J.K., 1999, *MNRAS* 308, 539
- Dent W.R.F., Matthews H.E.M., Walther D.M., 1995, *MNRAS* 277, 193
- Draine B.T., Roberge W.G., 1982, *ApJ* 259, L91
- Draine B.T., Roberge W.G., Dalgarno A., 1983, *ApJ* 264, 485
- Eislöffel J., Davis C.J., Ray T.P., Mundt R., 1994, *ApJ* 422, L91
- Eislöffel J., Mundt R., 1994, *A&A* 284, 530
- Eislöffel J., Smith M.D., Davis C.J., Ray T.P., 1996, *AJ* 112, 2086
- Evans N.J., Balkum S., Levreault R.M., Hartmann L., Kenyon S., 1994, *ApJ* 424, 793
- Everett M.E., DePoy D.L., Pogge R.W., 1995, *AJ* 110, 1295
- Fernandes, A.J.L., Brand, P.W.J.L. 1995, *MNRAS* 274, 639
- Garnavich P.M., Noriega-Crespo A., Raga A.C., Böhm K.-H., 1997, *ApJ* 490, 752
- Gredel R., 1994, *A&A* 292, 580
- Gredel R., 1996, *A&A* 305, 582
- Hartigan P., Morse J.A., Heathcote S., Cecil G., 1993, *ApJ* 414, L121
- Harvey P.M., Gatley I., 1983, *ApJ* 269, 613
- Hester J.J., Stapelfeldt K.R., Scowen P.A., 1998, *AJ* 116, 372
- Hollenbach D.J., McKee C.F., 1989, *ApJ* 342, 306
- Mac Low M.-M., Smith M.D., 1997, *ApJ* 491, 596
- McCartney M.S.K., Brand P.W.J., Burton M.G., Chrysostomou A., 1999, *MNRAS* 307, 315
- Micono M., Davis C.J., Ray T.P., Eislöffel J., Shetrone M.D., 1998, *ApJ* 494, L227
- Moro-Martín A., Cernicharo J., Noriega-Crespo A., Martín-Pintado J., 1999, *ApJ* 520, L111
- Neufeld D.A., McKee C.F., 1988, *ApJ* 331, L87
- Noriega-Crespo A., Garnavich P.M., 1994, *AJ* 108, 1432
- Noriega-Crespo A., Garnavich P.M., Curiel S., Raga A.C., Ayala S., 1997, *ApJ* 486, L55
- Olberg M., Reipurth B., Boots R.S., 1992, *A&A* 259, 252
- Oliva E., Origlia L., 1992, *A&A* 254, 466
- Ramsay S.K., Chrysostomou A., Geballe T.R., Brand P.W.J., Mountain M., 1993, *MNRAS* 263, 695
- Reipurth B., Heathcote S., Yu K.C., Bally J., Rodríguez L., 2000, *ApJ*, in press
- Schwartz R.D., Schultz A.S.B., Cohen M., Williams P.M., 1995, *ApJ* 446, 318
- Smith M.D., 1994, *MNRAS* 289, 256

- Smith M.D., 1995, *A&A* 296, 789
Smith M.D., Brand P.W.J., 1990a, *MNRAS* 243, 498
Smith M.D., Brand P.W.J., 1990b, *MNRAS* 245, 108
Smith M.D., Brand P.W.J., Moorhouse A., 1991a, *MNRAS* 248, 451
Smith M.D., Brand P.W.J., Moorhouse A., 1991b, *MNRAS* 248, 730
Smith M.D., Mac Low M.-M., 1997, *A&A* 326, 801
Smith M.D., Davis C.J., Lioure A., 1997a, *A&A* 327, 1206
Smith M.D., Suttner G., Zinnecker H., 1997b, *A&A* 320, 325
Smith M.D., Mac Low M.-M., Heitsch F., 2000b, *A&A*, submitted
Smith M.D., Mac Low M.-M., Heitsch F., 2000c, *A&A*, in prep.
Smith M.D., Mac Low M.-M., Zuev J., 2000a, *A&A* 356, 287
Solf J., Böhm K.H., 1991, *ApJ* 375, 618
Völker R., Smith M.D., Suttner G., Yorke H.W., 1999, *A&A* 343, 953
Wardle M., 1990, *MNRAS* 246, 98